Doppler asymmetric spatial heterodyne spectroscopy (DASH): concept and experimental demonstration

Christoph R. Englert,[1,*] David D. Babcock,[2] and John M. Harlander[3]

[1]U.S. Naval Research Laboratory, Space Science Division Code 7641, 4555 Overlook Avenue Southwest, Washington, District of Columbia 20375, USA
[2]Artep, Inc., 2922 Excelsior Springs Court, Ellicott City, Maryland 21042, USA
[3]Department of Physics, Astronomy, and Engineering Science, St. Cloud State University, 720 Fourth Avenue South MS-315, St. Cloud, Minnesota 56301, USA

*Corresponding author: Christoph.Englert@nrl.navy.mil

We describe the concept of Doppler asymmetric spatial heterodyne spectroscopy (DASH) and present a laboratory Doppler-shift measurement using an infrared laser line. DASH is a modification of spatial heterodyne spectroscopy optimized for high precision, high accuracy Doppler-shift measurements of atmospheric emission lines either from the ground or a satellite. We discuss DASH design considerations, field widening, thermal stability and tracking, noise propagation, advantages, and trade-offs. DASH interferometers do not require moving optical parts and can be built in rugged, compact packages, making them suitable for space flight and mobile ground instrumentation.   © 2007 Optical Society of America

OCIS codes: 300.6300, 120.6200, 120.2650.

1. Introduction

Historically, Doppler-shift measurements of atmospheric emission lines have been used to derive atmospheric wind speed and direction using ground-based and satellite instruments. Satellite measurements provide global scale coverage, yet only few such instruments have been built and flown. Currently, global wind data for the middle and upper atmosphere are not routinely available, even though they are required for studying atmospheric dynamics and energetics and they are of critical importance for constraining global scale models [1]. Here we present a detailed discussion on the recently developed Doppler asymmetric spatial heterodyne spectroscopy (DASH) technique [2]. DASH combines advantages of state-of-the-art optical techniques while avoiding some of their limitations.

After a brief review of the DASH heritage, we describe the optical concept and the optimum optical path offset. We also include considerations important

for the choice of the Littrow wavenumber and the resolving power in the interferometer design. After discussing the DASH noise propagation we show that DASH interferometers can be field widened, which is essential for obtaining high sensitivity in a compact, rugged instrument suitable for space flight. After summarizing important DASH advantages and trade-offs, we present the first Doppler shift measurements made with a DASH interferometer.

2. Heritage

To date, space-based Doppler-shift observations of atmospheric emission lines have been made from a few research satellites to obtain wind information. Since the measured Doppler shift contains only velocity information along the line of sight, measurements of horizontal wind speed and direction require the observation of the same location using two perpendicular viewing directions. For a satellite in low Earth orbit, this is typically achieved by viewing the Earth's limb 45° and 135° from the ram direction of the satellite, which results in the observation of the

Report Documentation Page		*Form Approved* *OMB No. 0704-0188*

Public reporting burden for the collection of information is estimated to average 1 hour per response, including the time for reviewing instructions, searching existing data sources, gathering and maintaining the data needed, and completing and reviewing the collection of information. Send comments regarding this burden estimate or any other aspect of this collection of information, including suggestions for reducing this burden, to Washington Headquarters Services, Directorate for Information Operations and Reports, 1215 Jefferson Davis Highway, Suite 1204, Arlington VA 22202-4302. Respondents should be aware that notwithstanding any other provision of law, no person shall be subject to a penalty for failing to comply with a collection of information if it does not display a currently valid OMB control number.

1. REPORT DATE **2007**	2. REPORT TYPE	3. DATES COVERED **00-00-2007 to 00-00-2007**

4. TITLE AND SUBTITLE	5a. CONTRACT NUMBER
Doppler asymmetric spatial heterodyne spectroscopy (DASH): concept and experimental demosntration	5b. GRANT NUMBER
	5c. PROGRAM ELEMENT NUMBER
6. AUTHOR(S)	5d. PROJECT NUMBER
	5e. TASK NUMBER
	5f. WORK UNIT NUMBER

7. PERFORMING ORGANIZATION NAME(S) AND ADDRESS(ES) **Naval Research Laboratory,Space Science Division, Code 7641,4555 Overlook Avenue SW,Washington,DC,20375**	8. PERFORMING ORGANIZATION REPORT NUMBER

9. SPONSORING/MONITORING AGENCY NAME(S) AND ADDRESS(ES)	10. SPONSOR/MONITOR'S ACRONYM(S)
	11. SPONSOR/MONITOR'S REPORT NUMBER(S)

12. DISTRIBUTION/AVAILABILITY STATEMENT **Approved for public release; distribution unlimited**

13. SUPPLEMENTARY NOTES

14. ABSTRACT

15. SUBJECT TERMS

16. SECURITY CLASSIFICATION OF:			17. LIMITATION OF ABSTRACT	18. NUMBER OF PAGES	19a. NAME OF RESPONSIBLE PERSON
a. REPORT **unclassified**	b. ABSTRACT **unclassified**	c. THIS PAGE **unclassified**	**Same as Report (SAR)**	**11**	

Standard Form 298 (Rev. 8-98)
Prescribed by ANSI Std Z39-18

same location within several minutes and with two perpendicular fields of view.

Doppler wind observations from satellites have been made using either Fabry–Perot interferometers [3,4], a stepped Michelson interferometer [5], or a microwave spectrometer [6].

Fabry–Perot interferometers can measure wind field information and also allow density retrievals using line intensities in addition to temperature retrievals using line shapes and relative line intensities. The main technical challenges for the Fabry–Perot interferometers are the demanding fabrication and alignment tolerances ($\sim \lambda / 20$) and, in case of a satellite instrument, maintaining the alignment on orbit. The large resolving power that is required for wind measurements limits the throughput and drives the overall size of the instrument.

Stepped Michelson interferometers, also known as stepped Fourier transform spectrometers (FTS), use the fact that a small frequency shift of a single emission line results in a phase shift in the interferogram fringe pattern that increases with increasing optical path difference (OPD). For a single, isolated atmospheric emission line, this phase shift can be determined by measuring a small number of interferogram points. These points are ideally separated by a path difference of $\lambda / 4$ around a large OPD offset. Typically, four interferogram samples are measured using either a moving mirror [5,7] or a faceted mirror [8,9], which eliminates the moving parts in the interferometer. Stepped Michelson interferometers can be field widened and temperature compensated [10,11] to achieve the sensitivity and stability necessary for a satellite instrument. Data from stepped Michelson interferometers can also be used to obtain temperature data using line shape information, which is contained in the interferogram contrast [5]. A limitation of stepped Michelson interferometers is that the isolation of a single atmospheric emission line typically requires an ultranarrow prefilter with all its attendant difficulties and reduction in throughput. Further limitations are that the interferogram is only sampled at a few (typically four) OPDs and instrument drifts cannot be monitored simultaneous with every atmospheric measurement, since only one line may be in the passband at any time.

DASH can be considered a combination of stepped FTS and spatial heterodyne spectroscopy (SHS). The SHS concept is similar to a Michelson interferometer, but the interferometer arms are terminated by fixed, tilted gratings. SHS instruments measure all interferogram samples simultaneously in the spatial domain using a line or array detector. They heterodyne the spatial fringe frequency around the Littrow wavenumber, σ_L, of the gratings, which allows the optimum use of the number of array detector elements [12]. Detailed descriptions of the SHS concept and data analysis can be found in publications by Harlander *et al.* [12,13], Englert *et al.* [14], and Englert and Harlander [15]. SHS instruments can be field widened with fixed prisms and they can be built as

very compact, robust, and lightweight packages suitable for space flight [13].

3. DASH Concept

A. Optical Configuration

Typical atmospheric wind velocities cause atmospheric emission lines to be Doppler shifted by only a few parts in 10^8. This small wavelength shift results in a small frequency change in the interferogram as recorded by an SHS, DASH, or FTS instrument. Figure 1 shows an ideal interferogram of a single, infinitely narrow spectral line versus OPD and the interferogram of a slightly Doppler-shifted line. As is well known, the small frequency change in the interferogram has a negligible effect for small OPDs; however, at longer path differences it appears predominantly as a phase shift. The main objective of DASH is to measure this phase shift; thus, it is sufficient to measure the interferogram at high OPDs. Note that the brightness of the interferogram and the fringe contrast contain information about the density of the emitter and the line shape, just as in the stepped FTS case [5].

The phase shift, $\delta\varphi$, of a single emission line as a function of the OPD, $2\Delta d$, or interference order, $k = 2\Delta d\sigma$, can be written as [5]:

$$\delta\varphi = 4\pi\Delta d\sigma(v/c) = 2\pi k(v/c), \qquad (1)$$

where σ is the non-Doppler-shifted wavenumber of the emission line, v is the Doppler velocity, and c is the speed of light.

Using the configuration illustrated in Fig. 2, DASH allows the measurement of the interferogram within a path difference interval around the path difference offset $2\Delta d$. The DASH concept is a slight modification of the SHS concept [12]. The only difference is the additional optical path offset in one arm, which makes the interferometer asymmetric. Like SHS, DASH can be explained assuming a plane wavefront entering the interferometer shown as the vertical dashed line in Fig. 2. The wavefront is split at the beam splitter so that the two resulting beams illumi-
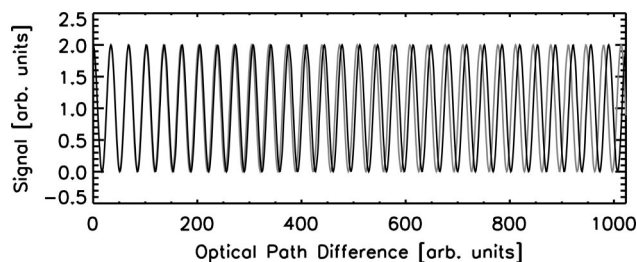

Fig. 1. Black: Interferogram of an infinitely narrow spectral line. Gray: Interferogram of a slightly Doppler-shifted, infinitely narrow spectral line. This figure shows that the high resolution information about the exact line position and therefore the Doppler shift of the line is contained at high optical path differences. At large OPDs, the predominant effect is a phase shift between the two fringe patterns that have slightly different frequencies.
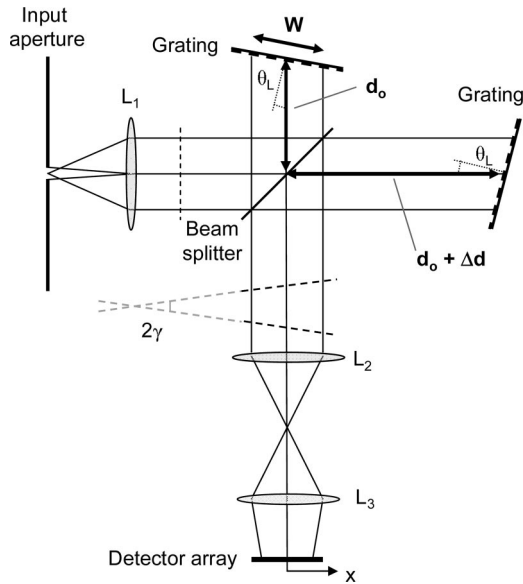
Fig. 2. Schematic of a non-field-widened DASH interferometer. The only difference between a conventional SHS interferometer and a DASH interferometer is the additional OPD offset ($2\Delta d$) in one of the interferometer arms.

nate the gratings at the end of the interferometer arms. After being diffracted at the gratings, the wavefronts return to the beam splitter and recombine. At this point, the two wavefronts are each tilted by the angle $\gamma \approx 2\tan\theta_L[(\sigma - \sigma_L)/\sigma]$ with respect to the optical axis, and one wavefront is delayed by the optical path offset $2\Delta d$. Due to the wavelength-dependent tilt of the wavefronts caused by the gratings, the detector array records a wavenumber-dependent Fizeau fringe pattern, which is the Fourier transform of the incident spectral density heterodyned around the Littrow wavenumber $\sigma_L = 1/(2g\sin\theta_L)$, where $1/g$ is the groove density of the gratings. The interferogram recorded by the DASH array detector can generally be written as

$$I(x) = \frac{1}{2}\int_0^\infty B(\sigma)\left[1 + \cos\left\{2\pi[4(\sigma - \sigma_L)\tan\theta_L\right.\right.$$
$$\left.\left. \times\left[x + \frac{\Delta d}{2\tan\theta_L}\right]\right\}\right]d\sigma, \qquad (2)$$

where x is the location on the detector array as indicated in Fig. 2 ($x = 0$ is the center of the array), θ_L is the Littrow angle of the gratings, $B(\sigma)$ is the spectral density of the incident radiation, and the magnification of the imaging optics (L_2 and L_3 in Fig. 2) is assumed to be unity. The sampled path difference interval, d, is

$$2(\Delta d - W\sin\theta_L) < d < 2(\Delta d + W\sin\theta_L), \qquad (3)$$

where W is the beam width measured along each grating. The effective resolving power can be found using $R = \sigma(4W\sin\theta_L) \approx 2W/g$. The resolving power

is equivalent to the number of illuminated grating grooves. This is the same result as for conventional SHS [12].

In contrast to the typical stepped Michelson interferometer, DASH allows the simultaneous measurement of several hundred interferogram samples within the path difference interval defined in Eq. (3). This means that DASH can simultaneously measure multiple lines, including calibration lines that can be used to track instrumental drifts.

B.   Optimum Path Difference Offset

Atmospheric emission lines are subject to line broadening effects such as pressure and temperature broadening. Line broadening affects the envelope of the interferogram; a broader line corresponds to an envelope that decreases more rapidly with increasing path difference. In general, this envelope function causes the interferogram contrast, or visibility, to decrease with increasing OPD, as shown for a purely temperature broadened line in Fig. 3. This effect competes with the increasing phase shift for increasing optical path difference [see Eq. (1)] so that there is an optimum path difference offset for which measuring the phase shift and thus the Doppler shift is most sensitive. We find this optimum path difference by maximizing the envelope of the difference between the interferograms of a Doppler-shifted and a Doppler-non-shifted line (see Fig. 3). Maximizing the envelope, rather than the actual interferogram differences, is appropriate since the DASH concept allows the simultaneous observation of many fringes, as will be discussed in Section 4. For the example of a purely temperature broadened line, which has a Gaussian line shape proportional to $\exp[-(\sigma - \sigma_0)^2/2\sigma_D^2]$ and a width of

$$\sigma_D = \sigma_0\sqrt{\frac{kT}{mc^2}}, \qquad (4)$$

the optimum path difference is

$$2\Delta d_{OPT} = \frac{1}{2\pi\sigma_D}, \qquad (5)$$
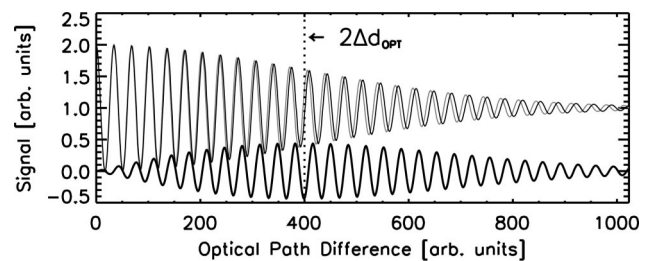

Fig. 3. Thin black: Interferogram of a single, temperature broadened curve. The decreasing contrast for increasing OPD is due to the finite line width of the emission curve. Thin gray: Interferogram of slightly Doppler-shifted emission curve. Thick black: Difference between the two interferograms. The dotted vertical line indicates the OPD for which the envelope of the difference function is largest. Here, the measurement is most sensitive to the phase shift.

where T is the temperature, m is the mass of the emitter, σ_0 is the wavenumber of the line center, and k is the Boltzmann constant. Although Eq. (5) predicts the optimum path difference about which to make a Doppler measurement, practical concerns such as the size and sensitivity of the instrument may require the instrument be build with a nonoptimum, typically smaller, path difference.

Finally, we point out that the optimum path difference only depends on the emission line shape. This is the case even if more than one line is within the passband, as will be discussed in Section 4.

C. Phase (Doppler Shift) Determination

We can simplify the DASH interferogram from several emission lines by writing

$$
\begin{aligned}
I_D(x) &= \sum_j S_j[1 + E_j(x)\cos(2\pi\kappa_j x + \Phi_j + \delta\varphi_j)] \\
&= \sum_j S_j\Bigg(1 + \frac{1}{2}E_j(x)\{\exp[i(2\pi\kappa_j x + \Phi_j + \delta\varphi_j)] \\
&\quad + \exp[-i(2\pi\kappa_j x + \Phi_j + \delta\varphi_j)]\}\Bigg),
\end{aligned}
\tag{6}
$$

where j indexes several lines in the passband, x is the location on the detector as shown in Fig. 2, S_j is proportional to the line brightness, $E_j(x)$ are the envelope functions that depend on the individual line shape and the path difference offset, $\kappa_j \equiv 4(\sigma_j - \sigma_L)\tan\theta_L$ are the heterodyned spatial fringe frequencies for each line center, σ_j, $\Phi_j \equiv 4\pi(\sigma_j - \sigma_L)\Delta d$ are additive phase terms, and $\delta\varphi_i$ are the phase shifts resulting from the Doppler shift of each line. Note that κ also changes with the Doppler shift of the line, but that effect is typically negligible for typical atmospheric wind speeds.

When the bandpass, Littrow wavenumber, and path difference interval are chosen appropriately (see Section 4), the Fourier transform of Eq. (6) yields a complex spectrum with localized, well-separated features around spatial frequencies $+\kappa_j$ and $-\kappa_j$. The next step is to isolate one of these features, e.g., $j = 0$, by zeroing out all spectral elements (including the ones at $-\kappa_0$) except the ones within a local region around $+\kappa_0$. This step effectively eliminates all interferogram contributions [see Eq. (6)], except one of the exponential terms, so that after the inverse Fourier transform we get

$$
\begin{aligned}
I_D^0(x) &= \frac{1}{2}S_0 E_0(x)\exp[i(2\pi\kappa_0 x + \Phi_0 + \delta\varphi_0)] \\
&= \frac{1}{2}S_0 E_0(x)[\cos(2\pi\kappa_0 x + \Phi_0 + \delta\varphi_0) \\
&\quad + i\,\sin(2\pi\kappa_0 x + \Phi_0 + \delta\varphi_0)].
\end{aligned}
\tag{7}
$$

Using Eq. (7), the phase term can now be calculated from the ratio of its imaginary and its real part [14,16]:

$$
2\pi\kappa_0 x + \Phi_0 + \delta\varphi_0 = \arctan\left(\frac{\Im(I_D^0)}{\Re(I_D^0)}\right).
\tag{8}
$$

After subtraction of $2\pi\kappa_0 x + \Phi_0$, which is also called the zero wind phase, we get the phase shift $\delta\varphi_0$ caused by the Doppler shift for this particular line. The speed between the emitter and the spectrometer can now be calculated using the phase shift $\delta\varphi_0$ and Eq. (1). The procedure can be applied for all lines in the passband ($j = 0, 1, \ldots$), yielding an independent velocity measurement for each line.

We point out that the subtraction of the zero wind phase is a very critical step, since the zero wind phase is likely to be sensitive to instrument drifts. One method to determine the zero wind phase is to simultaneously observe a known, non-Doppler-shifted reference line. With DASH one can, for example, use an *in situ* calibration lamp that has one or more spectral lines in the passband and superimpose its signal onto the observed scene with an additional beam splitter. This way every exposure includes a simultaneous zero wind calibration (see also Section 7).

4. Choice of Passband, Littrow Wavenumber, and Resolving Power

To optimize the sensitivity of the atmospheric wind measurement, the choice of the passband depends on many factors such as the targeted emission spectrum, radiative transfer considerations, and/or detector performance, to name only a few. Here, we focus on the considerations that are generally important for a DASH instrument rather than specific to a particular application.

First, one or more emission lines must be identified. If more than one line is chosen, they need to be well separated, i.e., their spectral spacing should be at least several times their linewidth. Second, the Littrow wavenumber and resolving power are chosen, which will constrain the number of illuminated grating grooves, the groove density, and the grating angle (see Subsection 3.A) of the DASH interferometer. The choice should be made so that the observed emission lines correspond to well-separated spatial frequencies that can be easily isolated in the spectral domain as described in Subsection 3.C. For example, assuming a resolving power of 6000, a Littrow wavenumber of $6000\ \mathrm{cm}^{-1}$, and three emission lines at 6020, 6060, and $6085\ \mathrm{cm}^{-1}$, the interferogram consists of roughly 20, 60, and 85 fringes, respectively, across the detector. To avoid aliasing, the highest fringe frequency may not exceed the Nyquist frequency, that is, the number of fringes across the detector width may not exceed the number of detector pixels divided by 2. This example illustrates that the heterodyning aspect of DASH is essential for achieving well-separated fringe frequencies that can easily be sampled by available detector arrays that typically have hundreds of pixels. Without heterodyning, the fringe frequencies would be proportional to the line positions in wavenumbers, so that in the cited example, the fringe frequencies of the lines at 6060 and

6085 cm^{-1} would differ by less than 0.5% (see also Section 6). Choosing fringe frequencies that are well separated also ensures that the envelope of the beat pattern from two or more lines in the passband has a periodicity that is significantly smaller than the width of the detector. This way the interferogram sampled by the detector can never be confined to a region near a node or zero point of the beat pattern envelope, which would result in greatly reduced contrast for the entire interferogram. Rather, the optimum path offset remains a function of the line shape only (see Subsection 3.B).

The passband is typically defined by an optical filter in the DASH instrument. It is very important to note that the DASH filter is not required to isolate a single line in the observed emission line spectrum, such as in the case of a stepped Michelson interferometer. This generally allows the usage of a broader filter, with significantly higher peak transmittance as well as less angular and thermal dependence of the transmittance, which results in higher etendue and therefore higher sensitivity of the instrument.

5. Noise Propagation

To estimate the Doppler velocity sensitivity of a DASH instrument, one needs to estimate the precision of the phase retrieval [see Eq. (1)]. Here, we specifically describe the noise propagation from the measured interferogram to the retrieved phase [see Eq. (8)].

We start with the random noise, ε_I, of the dark and flat field corrected [15] interferogram. For a photon shot-noise-limited detector array and perfect fringe contrast, one can estimate, for example,

$$\varepsilon_I = \sqrt{\frac{I_{\text{tot}}}{N} + \varepsilon_r + \varepsilon_d}, \qquad (9)$$

where I_{tot} is the total number of detected electrons in the interferogram, N is the number of interferogram samples (e.g., number of pixels in a row of the focal plane array), ε_r is the read noise component, and ε_d is the dark noise component. After Fourier transformation into the spectral domain, the random noise in the interferogram propagates to random noise in the real and imaginary part of the spectrum with a distribution width of

$$\varepsilon_S = \frac{1}{\sqrt{N}} \varepsilon_I. \qquad (10)$$

After isolating the localized spectral feature of one emission line with a boxcar function that is n pixels wide, centered on the feature, and subsequent inverse Fourier transformation into the interferogram domain, the distribution width of the random noise in both the real and imaginary part of the isolated interferogram can be written as

$$\varepsilon_I^{\text{ISO}} = \frac{\sqrt{n}}{\sqrt{N}} \varepsilon_I. \qquad (11)$$

It is important to point out that the line isolation with the boxcar function results in noise in the interferogram that is no longer uncorrelated from sample to sample. Only n samples remain uncorrelated; the others result from their interpolation.

Propagating the correlated noise of the isolated interferogram through Eq. (8) results in the magnitude of the correlated noise in the retrieved phase, $\varepsilon_P^{\text{ISO}}$, in units of radians:

$$\varepsilon_P^{\text{ISO}} = \frac{\varepsilon_I}{A_i} \sqrt{\frac{2n}{N}} = \frac{\varepsilon_I}{I_i} \sqrt{2Nn}, \qquad (12)$$

where A_i is the amplitude of the fringe for the isolated line i in the measured interferogram and I_i is the total modulated signal detected in the interferogram for the isolated line i. Other potential sources of error include systematic and random uncertainties from the zero wind phase subtraction or pointing errors of a satellite platform, which can result in the improper correction for the satellite velocity.

6. Field-Widened DASH

The maximum field of view that can be accepted by any interferometer, and therefore its sensitivity for diffuse sources, is determined by how the interferometric path difference varies with off-axis angle. To minimize this variation and achieve a maximum possible field of view SHS instruments can be field widened by placing fixed prisms in each arm of the
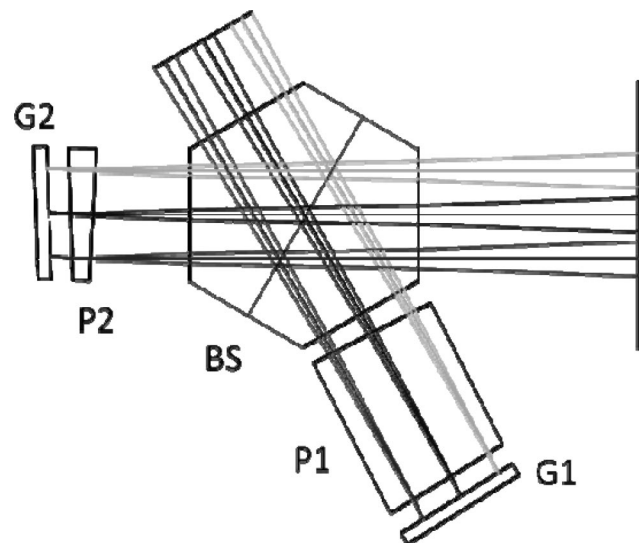

Fig. 4. Schematic of field-widened DASH interferometer for the near-infrared (BS: beam splitter, G1/2: gratings, P1/2: field widening prisms). Field widening is obtained by placing fixed prisms in each interferometer arm. The thicker prism (P1) in the lower right arm is required to compensate for the larger path difference. The grating and prism angles are the same in each arm.

Table 1. Interferometer Specifications and Performance

Path difference offset Δd	6.5 cm
Path difference interval sampled	± 0.39 cm
Grating angle	5.6°
Resolving power at maximum path	110,000
Solid angle gain due to field widening	450×
Littrow wavelength	1.266 μm

interferometer [12]. The field of view for a field-widened SHS depends on the prism angle and is generally larger for smaller prism angles [12]. The maximum solid angle that can be accepted by a field-widened SHS is typically 2 orders of magnitude larger than interferometers without field widening. The resulting increase in sensitivity is critical for high spectral resolution geophysical measurements where signals can be weak and/or are obscured by large background signals. Field-widening techniques have also been used with stepped FTS; however, in this case plane-parallel blocks of glass are used instead of prisms [5]. Figure 4 is a schematic of a field-widened DASH interferometer designed, as an example, to measure four atmospheric $O_2^1\Delta$ lines in the near-infrared (NIR) at wavelengths approximately 1.250 μm. The prism and grating angles in the two arms are the same; however, the prism in the lower right-hand portion of the figure is thicker to compensate the larger optical path in this arm. As indicated earlier, this system can be considered as a symmetric field-widened SHS with an offset aperture.

Table 1 indicates key specifications and the optical performance of this interferometer as determined by ray tracing. Note in particular that the field-widening prisms enable the system to view a solid angle that is approximately 450 times larger than a non-field-widened system of the same resolution. Table 2 lists four targeted $O_2^1\Delta$ lines near $\lambda = 1.250$ μm along with the number of fringes each line produces across the full aperture of the DASH interferometer. The last column indicates the number of fringes a non-heterodyned Michelson interferometer would need to record over the same path difference interval. The smaller number of fringes for the SHS and DASH enables sampling of the interferogram with a practical detector having hundreds of pixels. To simultaneously measure these four lines with a stepped Michelson interferometer a prefilter must be used to spatially separate each line on a different portion of the detector [17], which adds complexity and reduces the sensitivity of the measurement.

7. Phase Stability

Michelson-based instruments, including ones that use the DASH concept, depend on measuring the absolute phase of the fringe pattern to determine the Doppler wind velocity. As a result one of the most challenging aspects of these measurements is the calibration and tracking of instrument drifts that affect the phase measurement. The drifts can be minimized by appropriate thermal compensation within the interferometer. In addition, active thermal control is possible as well as periodic measurements of a calibration source to determine the zero wind reference. All of these techniques have been implemented previously (e.g., on the WINDII instrument [5,11]) and can be readily adapted to DASH. Since DASH can measure many lines simultaneously, the calibration source can be observed during an exposure that eliminates difficulties associated with alternating exposures between science and calibration images.

8. Advantages and Trade-Offs

The following is an itemized list of the most important advantages and trade-offs of the DASH concept for measuring atmospheric wind:

No moving parts: Like SHS interferometers, DASH interferometers do not require any moving optical components and can be built in a compact, robust way, which makes them highly suitable for space flight [13].

Etendue: Like the stepped Michelson technique, DASH has large interferometric throughput and can be field widened [5].

Multiline capability: DASH interferometers can observe multiple emission lines simultaneously in the passband, which eliminates the use of ultranarrow filters and the associated reduction in throughput and temperature sensitivity. Note that accepting multiple lines into the interferometer does have an impact on the multiplex noise as outlined in Section 5, due to the increase in total signal, I_{tot}. Typically, however, the multiline benefit outweighs the multiplex penalty since the noise in the phase determination is proportional to the square root of the total signal [see Eqs. (9) and (12)].

Simultaneous phase tracking: The capability to simultaneously observe multiple lines allows the tracking of the zero wind phase by superimposing a known emission line onto the atmospheric scene.

Increased immunity to ghosts and background features: Since DASH records several hundred interferogram points within an OPD interval centered on a path offset, one gains increased immunity to ghost fringes and background features.

Thermal drifts: Just as for stepped Michelson interferometers and Fabry–Perot interferometers, thermal effects on the measured phase are expected to be significant. To mitigate these effects the interferometer can be designed using materials that provide

Table 2. Targeted Lines Near $\lambda = 1.250$ μm

Wavelength [μm]	Number of Fringes for ± 0.39 cm Path Interval	
	Heterodyned (DASH, SHS)	Not Heterodyned (e.g., FTS)
1.252644	65.7	9770.6
1.254210	57.9	9782.8
1.255809	50.0	9795.3
1.257439	41.9	9808.0

maximum thermal compensation, as has been successfully demonstrated for stepped Michelson interferometers [5,11]. In addition, the above-mentioned simultaneous phase tracking may be used to quantify and ultimately correct the remaining thermal effects.

One-dimensional imaging: Like stepped Michelson interferometers and Fabry–Perot interferometers, DASH can be designed for one-dimensional imaging using a two-dimensional detector array. For a space-based instrument this means that no limb scanning is required in order to measure a vertical wind profile.

9. Experimental Demonstration

A. Overview

A non-field-widened breadboard DASH interferometer was built and used to measure the Doppler shift of a laboratory line source for a typical upper atmospheric wind speed. The line source and the passband of the instrument were chosen to be in the NIR (~ 1.5 μm) since there are atmospheric emission lines close to this wavelength region that are suitable for wind measurements on Earth and other planets [17,18]. The DASH breadboard was constructed using predominantly commercial off-the-shelf (COTS) components.

B. Instrument Description

The laboratory setup consists of two major parts, the line source and the spectrometer. A diode laser beam that is reflected from a spinning wheel provides a collimated source that can be alternated between Doppler shifted and non-Doppler shifted using a chopper wheel. The spectrometer includes the DASH interferometer, exit optics, and an array detector. The principal components of the breadboard are described in Table 3.

A schematic of the source setup is shown in Fig. 5. The signal from a 40 mW, single-mode, temperature-controlled diode laser with $\sigma \simeq 6630$ cm^{-1}, passes through an optical isolator to prevent back coupling into the laser cavity. After the isolator, the beam is collimated and sent through a beam splitter to a chopper wheel. The chopper wheel is covered with retroreflecting tape so that a non-Doppler-shifted beam is reflected back to the beam splitter when the chopper blade blocks the optical path to the spinning disk (or Doppler wheel). The Doppler wheel is an aluminum disk, also coated with retroreflecting tape that is mounted at an angle to the optical axis. It rotates in order to produce a Doppler shift in the retroreflected beam. The beam returning from the Doppler wheel is subsequently reflected by the beam splitter and coupled back into an optical fiber via a focusing lens. This fiber serves as the input to the interferometer.

The optical layout of the interferometer is shown in Fig. 2 where the path difference Δd was set to 7.75 cm. A photograph of the breadboard interferometer and Doppler wheel is shown in Fig. 6. The interferom-

Table 3. Principal Breadboard Components

Component	Parameter	Description
Line source		
Laser diode	Manufacturer (Model)	Furukawa (FOL15DCWD-A81)
	Nominal wavelength	1528.78 nm
	Output power	40 mW
	Line width	1 MHz
	Operating temperature	Nominal: 25 °C
Interferometer		
Beam splittter	Manufacturer (Model)	Thorlabs (BS015)
	R:T	50:50 nonpolarizing
	Flatness	1/10 at 635 nm
	Size	25.4 mm^3 (cube)
Gratings	Manufacturer	Newport Corporation
	Grooves density	300 mm^{-1}
	Blaze angle	14.77°
	Blaze wavelength	1.71898 μm
	Coating	Gold
	Ruled area	26 mm × 26 mm
Detector		
InGaAs camera	Manufacturer (Model)	Xenics (XEVA-FPA-1.7-320)
	Array size	320 × 256 pixel
	Pixel pitch	30 μm
	Wavelength range	0.9–1.7 μm
	D*	7.5×10^{12} cm Hz$^{1/2}$/W
	Dynamic range	12 bit

eter was vibrationally isolated from the optical bench, and a top cover was used to suppress ambient and stray light contributions.
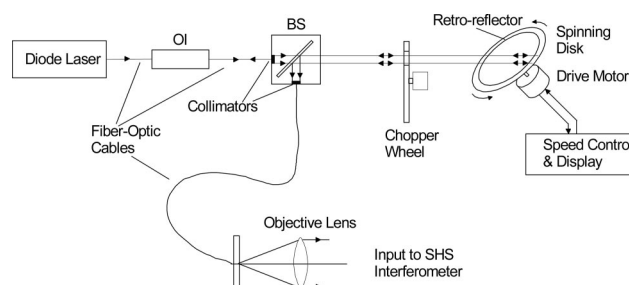

Fig. 5. Schematic of the laboratory setup. The monochromatic signal from a laser diode is guided by an optical fiber through an optical isolator and collimated by a single lens. The collimated beam is transmitted by a beam splitter and a chopper wheel and reflected by retroreflecting tape on a spinning disk that is mounted at an angle with respect to the optical axis. The Doppler-shifted signal from the spinning disk returns back through the chopper and is reflected by the beam splitter and then coupled into an optical fiber that guides the signal to the collimator feeding the interferometer (see also Fig. 2). The chopper blade is also coated with retroreflecting tape so that a non-Doppler-shifted signal enters the interferometer when the chopper is closed.
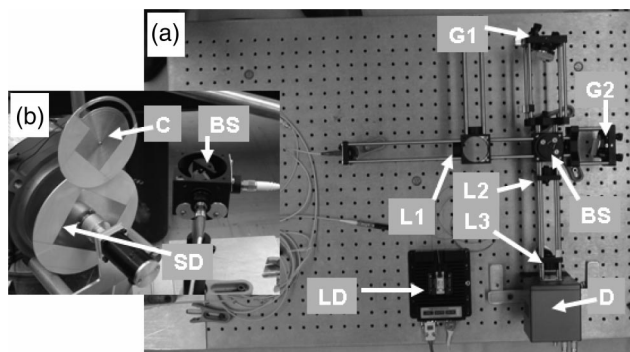
Fig. 6. Photographs of the laboratory setup showing the source and interferometer part; (a) shows the laser diode (LD) at the bottom center. The light from the laser is directed by an optical fiber to a beam splitter which is shown on the right of the inset (b). After being transmitted by this beam splitter, the signal is retro-reflected either by the chopper wheel (C) or the spinning disk (SD), which imposes a Doppler shift to the incident beam. The returning beam is then reflected by the beam splitter and coupled into a fiber that feeds the interferometer via a collimating lens (L1). The interferometer is set up analogous to Fig. 2 with the two gratings, G1/2, the beam splitter, BS, the exit optics, L2/3, and the detector array, D.

C. Results

Single line: Figure 7 shows a typical fringe image or interferogram as obtained by the DASH breadboard instrument when viewing a monochromatic source. As expected from Eq. (2), the image shows a cosine fringe pattern with a single spatial frequency across the detector. The image has been dark corrected and flat-field corrected [15].

The upper panel of Fig. 8 shows the intensity within a single row of a measured interferogram. The middle panel of Fig. 8 shows the real and imaginary part of the Fourier transform of this interferogram. The salient features of this complex spectrum are the lines around $\pm\kappa_0 = \pm 64$ fringes per detector width. This is the fringe frequency produced by the wavelength of the laser diode. Following the procedure described in Subsection 3.C, the phase of the inter-
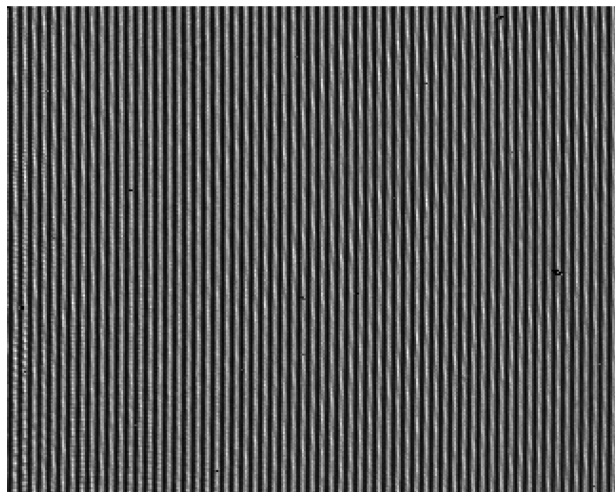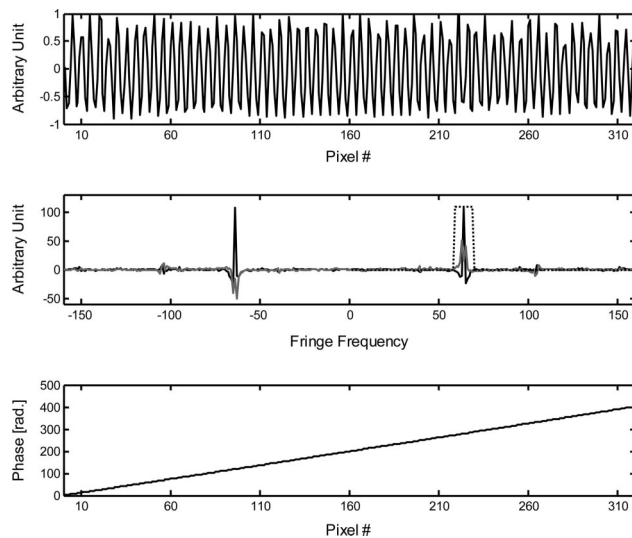

Fig. 8. Top panel: One pixel row from a single dark, flat-field, and offset corrected fringe image for a monochromatic source (see Fig. 7). Middle panel: Fourier transform of the interferogram shown in the top panel. The real part is shown in black; the imaginary part is shown in gray. The boxcar isolation function is shown with a dotted line (see text). Bottom panel: Phase of the interferogram shown in the top panel.

ferogram can be determined. A change in phase is a measure of a shift in line position and thus Doppler velocity. The isolation of the feature near $+\kappa_0$ is achieved by multiplying the complex spectrum with the boxcar function also shown in the middle panel of Fig. 8. The resulting phase of the interferogram is shown in the bottom panel of Fig. 8. For a Doppler-shifted line, the phase is expected to change according to Eq. (1). The phase shift of the fringe pattern along one detector row is a linear function of the OPD, and thus changes linearly across the recorded fringe pattern. Each pixel in the row provides a measure of a phase change due to the Doppler shift. A simple way to determine the phase shift between two fringe patterns is to compare the average phases across one single row. Subtracting these row averages yields the phase shift, $\delta\varphi$, in the middle of the recorded fringe pattern ($x = 0$), for which we defined the path offset Δd (see Fig. 2).

The top panel of Fig. 9 shows the row-averaged phases for each frame in a series of measurements taken at 100 measurements per second, where the average phase of the first measurement was subtracted from all subsequent ones. One can clearly see the regularly occurring phase shifts in the series that are a result of the chopped signal, alternating the Doppler-shifted signal and the reference, non-Doppler-shifted signal. One can also see a drift that is slowly varying compared to the sample rate. This drift is likely due to the control loop of the thermal stabilization of the laser. To measure the phase shift caused by the Doppler effect, the mean phase of the Doppler-shifted interferogram was subtracted from the mean phase of the non-Doppler-shifted interferogram. The results for several measurement series are

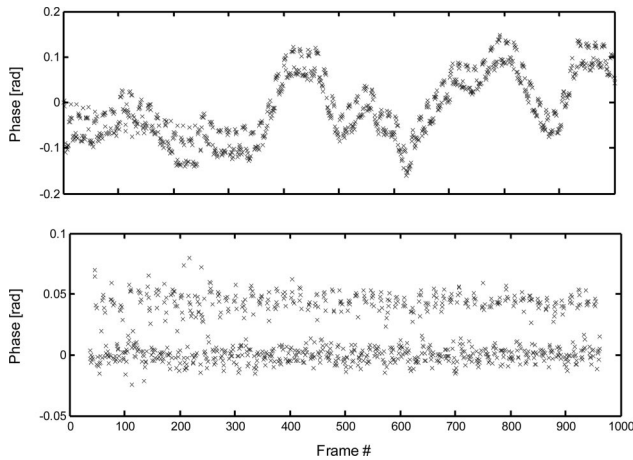Fig. 7. Typical dark and flat-field corrected fringe image.

Fig. 9. Top panel: Time series of the average phase of a single interferogram row where the average phase of the first measurement in the series is subtracted from all subsequent measurements. A periodic phase shift of ~0.05 rad caused by the chopped signal can clearly be seen in addition to a drift, which we attribute to the laser frequency stability. Bottom panel: drift corrected time series.
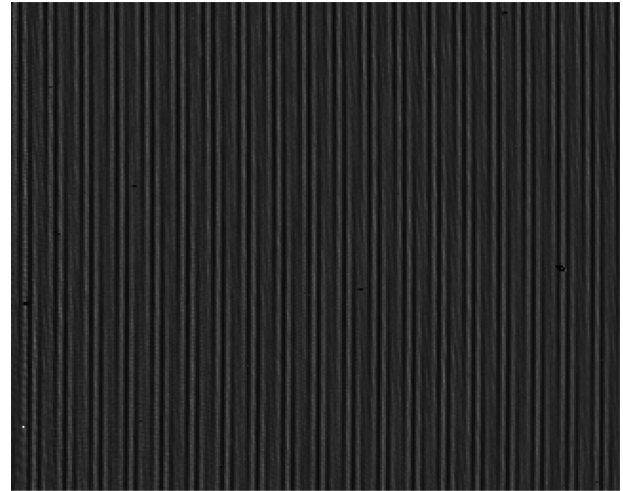

Fig. 10. Dark and flat-field corrected fringe image for two lines in the passband. Since the laboratory setup only has one monochromatic but tunable source, this image was obtained by adding two monochromatic fringe patterns for different laser frequencies and thus different fringe frequencies.

shown in Table 4 along with the Doppler speed, v, derived from the phase shift:

$$v = \frac{c\delta\varphi}{4\pi\Delta d\sigma}. \qquad (13)$$

The uncertainties quoted in Table 4 for the phase difference are the combined standard deviations of the two drift corrected measurement series as shown in the bottom panel of Fig. 9. They are a combination of the random noise in the interferogram propagated through the phase determination [see Eq. (12)] and systematic contributions. For this breadboard we estimate that the primary contribution to the systematic uncertainty is due to the slow drift, which we attribute mainly to the frequency stabilization of the laser. Other contributors to the uncertainties are the thermal stability of the interferometer and the exit optics. Note that the stability of the source is not an issue for an atmospheric measurement. The thermal stability of a DASH interferometer and the exit optics can be tracked simultaneously with a known emission line source as described in Section 7.

For each measurement series in Table 4 the laser was thermally tuned to a slightly different wavelength so that the recorded fringe frequency was dif-

ferent. Also shown in Table 4 is the expected Doppler velocity, v, calculated from the angular velocity of the rotating retroreflecting disk, ω, the radial distance of the retro-reflected spot from the disk center, r, and the angle of the disk with respect to the incident beam, θ:

$$v = 2r\omega\cos(\theta). \qquad (14)$$

The results agree within <1.6 ms^{-1}, and demonstrate the first Doppler velocity measurement using the DASH technique. In the following we briefly discuss the data analysis for the multiple line case.

Multiple lines: An example of a flat fielded interferogram image with two lines in the passband is shown in Fig. 10. Instead of a cosine fringe with a single spatial frequency the interferogram is a beat pattern resulting from two cosine fringes with different spatial frequencies. Since our DASH breadboard only has one laser source, this image was created by adding two interferogram images, each recorded for a different, thermally tuned, laser frequency. Interferograms for a two line source could have been recorded simultaneously; however, such a source was not available to us.

Figure 11 shows one row of the two-line interferogram image in the upper panel and the complex spec-

Laser Temperature [°C]	Number of Fringes	Phase Shift [rad]	Speed Calculated from Phase Shift [m/s]	Speed Calculated from Angular Wheel Velocity [m/s]
67	53	0.039(09)	18.1	
42	62	0.043(10)	19.9	
30	66	0.044(12)	20.4	19.2
10	72	0.045(09)	20.8	

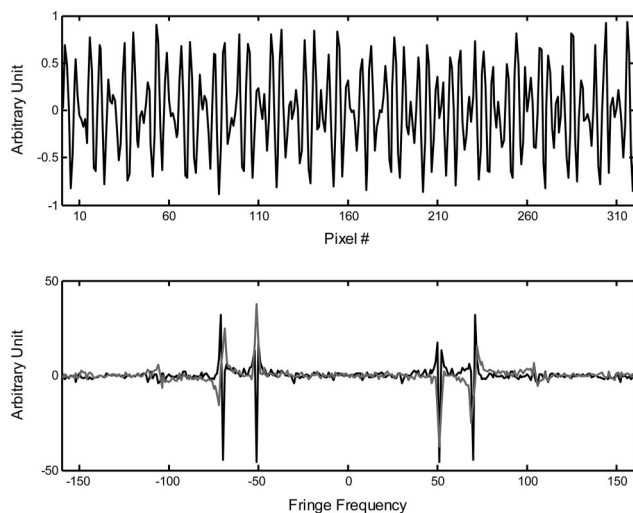**Table 4. Measurement Parameters and Results**

Fig. 11. Top panel: one pixel row from a single dark, flat-field, and offset corrected fringe image for two lines in the passband (see Fig. 10). Bottom panel: Fourier transform of the interferogram shown in the top panel. The real part is shown in black; the imaginary part is shown in gray.

trum in the bottom panel. Just as for the single-line case, each one of the lines can be isolated (e.g., with a boxcar function centered on the spectral feature). In case the instrumental line shape function contributions from the neighboring lines are considered to be a nonnegligible contribution, one can consider apodizing the interferogram, which helps to localize the spectral feature (i.e., suppress the line-shape contributions in the wings of the line). The remaining data processing to determine the phase is identical to the single-line case. This procedure can also be readily applied in the case of three or more lines in the passband as long as the spectral features are well separated so they can be isolated. A phase determination can be achieved for each line independently.

10. Conclusion

We have described the optical concept of Doppler asymmetric spatial heterodyne spectroscopy (DASH), a technique with heritage from conventional spatial heterodyne spectroscopy and stepped Michelson interferometers. DASH allows high precision, high sensitivity Doppler-shift measurements of emission lines and is therefore well suited for wind speed measurements in Earth's and other planetary atmospheres. We have shown how to determine the Doppler shift from the DASH interferogram phase shift. We have also shown how the measurement uncertainty in the interferogram propagates to the phase. Furthermore, we discussed specific DASH design parameters, such as the optimum path difference offset, passband, Littrow wavenumber, and resolving power. After covering field-widening aspects for DASH interferometers we summarized the most important advantages and trade-offs of DASH compared to stepped Michelson interferometers and Fabry–Perot interferometers. Two major advantages of DASH are that it does not require an ultranarrow optical filter that limits the

sensitivity and that a simultaneous calibration measurement can be performed to track instrument drifts. Finally, we reported the first measurement of a Doppler shift with a non-field-widened DASH laboratory breadboard.

References

1. W. A. Lahoz, R. Brugge, D. R. Jackson, S. Migliorini, R. Swinbank, D. Lary, and A. Lee, "An observing system simulation experiment to evaluate the scientific merit of the wind and ozone measurements from the future SWIFT instrument," Q. J. R. Meteorol. Soc. **131,** 503–523 (2005).
2. C. R. Englert, J. M. Harlander, D. D. Babcock, M. H. Stevens, and D. E. Siskind, "Doppler asymmetric spatial heterodyne spectroscopy (DASH): an innovative concept for measuring winds in planetary atmospheres," Proc. SPIE **6303,** 63030T (2006).
3. P. B. Hays, V. J. Abreu, M. E. Dobbs, D. A. Gell, H. J. Grassl, and W. R. Skinner, "The high-resolution Doppler imager on the upper atmosphere research satellite," J. Geophys. Res. **98,** 10713–10723 (1993).
4. T. L. Killeen, Q. Wu, S. C. Solomon, D. A. Ortland, W. R. Skinner, R. J. Niciejewski, and D. A. Gell, "TIMED Doppler interferometer: overview and recent results," J. Geophys. Res. **111,** A10S01, doi:10.1029/2005JA011484 (2006).
5. G. G. Shepherd, G. Thuillier, W. A. Gault, B. H. Solheim, C. Hersom, J. M. Alunni, J.-F. Brun, S. Brune, P. Charlot, L. L. Cogger, D.-L. Desaulniers, W. F. J. Evans, R. L. Gattinger, F. Girod, D. Harvie, R. H. Hum, D. J. W. Kendall, E. J. Llewellyn, R. P. Lowe, J. Ohrt, F. Pasternak, O. Peillet, I. Powell, Y. Rochon, W. E. Ward, R. H. Wiens, and J. Wimperis, "WINDII, the wind imaging interferometer on the upper atmosphere research satellite," J. Geophys. Res. **98,** 10725–10750 (1993).
6. D. L. Wu, M. J. Schwartz, J. W. Waters, V. Limpasuvan, Q. Wu, and T. L. Killeen, "Mesospheric Doppler wind measurements from aura microwave limb sounder (MLS)," Adv. Space Res., doi:10.1016/j.asr.2007.06.014 (2007).
7. W. A. Gault, S. Brown, A. Moise, D. Lang, G. Sellar, G. G. Shepherd, and J. Wimperis, "ERWIN: an E-region wind interferometer," Appl. Opt. **35,** 2913–2922 (1996).
8. W. A. Gault, S. Sargoytchev, and G. G. Shepherd, "Divided-mirror scanning technique for a small Michelson interferometer," Proc. SPIE **2830,** 15–18 (1996).
9. D. D. Babcock, G. G. Shepherd, W. E Ward, W. A. Gault, and S. Sargoytchev, "A prototype near-IR mesospheric imaging Michelson interferometer (MIMI) for atmospheric wind measurement," *Eos Trans. Am. Geophys. Union* **85,** Abstract SA41A-1040 (2004).
10. G. Thuillier and G. G. Shepherd, "Fully compensated Michelson interferometer of fixed path difference," Appl. Opt. **24,** 1599–1603 (1985).
11. G. Thuillier and M. Herse, "Thermally stable field compensated Michelson interferometer for measurement of temperature and wind of the planetary atmospheres," Appl. Opt. **30,** 1210–1220 (1991).
12. J. M. Harlander, R. J. Reynolds, and F. L. Roesler, "Spatial heterodyne spectroscopy for the exploration of diffuse interstellar emission lines at far-ultraviolet wavelengths," Astrophys. J. **396,** 730–740 (1992).

13. J. M. Harlander, F. L. Roesler, C. R. Englert, J. G. Cardon, R. R. Conway, C. M. Brown, and J. Wimperis, "Robust monolithic ultraviolet interferometer for the SHIMMER instrument on STPSat-1," Appl. Opt. **42,** 2829–2834 (2003).

14. C. R. Englert, J. M. Harlander, J. G. Cardon, and F. L. Roesler, "Correction of phase distortion in spatial heterodyne spectroscopy," Appl. Opt. **43,** 6680–6687 (2004).

15. C. R. Englert and J. M. Harlander, "Flatfielding in spatial heterodyne spectroscopy," Appl. Opt. **45,** 4583–4590 (2006).

16. J. M. Harlander, H. T. Tran, F. L. Roesler, K. Jaehnig, S. M. Seo, W. Sanders, and R. J. Reynolds, "Field widened spatial heterodyne spectroscopy: correcting for optical defects and new vacuum ultraviolet performance tests," Proc. SPIE **2280,** 310–319 (1994).

17. W. E. Ward, W. A. Gault, N. Rowlands, S. Wang, G. G. Shepherd, I. C. McDade, J. C. McConnell, D. Michelangeli, and J. Caldwell, "An imaging interferometer for satellite observations of wind and temperature on Mars, the Dynamic Atmosphere Mars Observer (DYNAMO)," Proc. SPIE **4833,** 226–236 (2002).

18. W. E. Ward, W. A. Gault, G. G. Shepherd, and N. Rowlands, "The waves Michelson interferometer: a visible/near-IR interferometer for observing middle atmosphere dynamics and constituents," Proc. SPIE **4540,** 100–111 (2001).